

Article

SAXS Analysis of Magnetic Field Influence on Magnetic Nanoparticle Clusters

Fábio Luís de Oliveira Paula 

Complex Fluid Group, Institute of Physics, University of Brasilia—UnB, Campus Darcy Ribeiro, Brasilia (DF) 70919-970, Brazil; fabioluis@fis.unb.br or fabioluis@unb.br; Tel.: +55-61-3107-7700

Received: 9 May 2019; Accepted: 16 June 2019; Published: 18 June 2019



Abstract: In this work, we investigated the local colloidal structure of ferrofluid, in the presence of the external magnetic field. The nanoparticles studied here are of the core-shell type, with the core formed by manganese ferrite and maghemite shell, and were synthesized by the coprecipitation method in alkaline medium. Measures of Small Angle X-ray Scattering (SAXS) performed in the Brazilian Synchrotron Light Laboratory (LNLS) were used for the study of the local colloidal structure of ferrofluid, so it was possible to study two levels of structure, cluster and isolated particles, in the regimes with and without applied magnetic field. In the methodology used here there is a combination of the information obtained in the system with and without magnetic field application. In this way, it is possible to undertake a better investigation of the colloidal dispersion. The theoretical formalism used: (i) the unification equation proposed by Beaucage G.; (ii) the analysis of the radial distribution function $p(r)$ and (iii) theoretical calculation of the radius of gyration as a function of the moment of inertia of the spherical of n -nanoparticles.

Keywords: Beaucage model; $\text{MnFe}_2\text{O}_{4+\delta}/\gamma\text{-Fe}_2\text{O}_3$ nanoparticles; D11-SAXS1 beamline

PACS: 61.05.cf; 78.67.Bf; 47.65.Cb; 81.16.Be; 05.45.Df

1. Introduction

Ferrofluids are a colloidal suspension of dispersions of magnetic nanostructures in a specific carrier liquid [1–3]. Together with the original conjunction of liquid and magnetic properties, ferrofluids can be confined, displaced, deformed and controlled by application of an external magnetic field. The applications of ferrofluids in the area of condensed matter are the most diverse due to their properties. These properties have aroused the interest of researchers in the field of chemistry and physics of condensed matter and in the development of nanotechnologies [4], in biomedical [5] and industrial applications. Recent studies have intensified the local colloidal structure in ferrofluids, and have mainly used the technique of small angle scattering; Fu et al. (2016) [6] investigated the self-assembly of supercrystals field-induced colloidal structure of core-shell NPs of core-shell iron oxide dispersed in toluene by small angle neutron scattering (SANS); Rozynek et al. (2011) [7] the effect of magnetic field on the structure formation in an oil-based magnetic fluid with various concentrations of magnetite particles by SAXS; Campi et al. (2019) [8] analyzed nanoparticles clusters of nickelate perovskite by $\text{S}\mu\text{XRD}$ (Scanning X-ray micro-Diffraction); Campi et al. (2019) [9] investigated hybrid nanoparticles diffusion and nanoscale aggregation, and observed how fractal dimensional changes leading to a mass surface fractal transition (SAXS); and Wandersman et al. (2015) [10] field induced anisotropic cooperativity in a magnetic colloidal glass. We can emphasize the study of the local colloidal structure with the objective of improving in the applications in the field of medicine, with specific use in hyperthermia in the treatment of cancer. In this context, we would like to highlight some works, pertinent to the influence of the colloidal organization of ferrofluids on the effect of hyperthermia: Myrovali et al. (2016) [11] has

verified the role of chain formation to further optimize the heating efficiency in the hyperthermia of Fe_3O_4 magnetic particles when magnetically aligned; Abenojar et al. (2016) [12] effect of nanochain and nanocluster formation on magnetic hyperthermia properties; Serantes et al. (2014) [13] observed that a system with chain-like arrangement biomimicking magnetotactic bacteria has the superior heating performance, increasing more than 5 times in comparison with the randomly distributed system when aligned with the magnetic field; Martinez-Boubeta et al. (2013) [14] heat generation of iron-oxide nanoparticles for magnetic hyperthermia; Mehdaoui et al. (2013) [15] increase of magnetic hyperthermia efficiency due to dipolar interactions in magnetic nanoparticles; and Bañobre-López et al. (2013) [16] use of magnetic nanoparticles-based hyperthermia in cancer therapy.

In order to investigate these properties in colloids, a Small Angle X-ray Scattering (SAXS) technique is very efficient. To analyze the scattering signal using a global dispersion function proposed by Beaucage G. [17,18], which unifies the local laws of Guinier and Porod in only one function that describes the form factor of a dispersion object in terms of radius of gyration and interfaces in the means. These models were successfully used to characterize a disordered cluster structure [19], a fractal mass of particles [20] as well as to distinguish between individual polydispersed particles and aggregates [21]. This work aims to investigate the local structure of magnetic colloids [22] under external magnetic field application, the colloids in question are composed of magnetic nanoparticles based on manganese ferrite type core-shell $\text{MnFe}_2\text{O}_{4+\delta}@\gamma\text{-Fe}_2\text{O}_3$ [23] and dispersed in aqueous medium. SAXS measurements were performed with external magnetic field applied [24] to determine the dimensions between nanoparticles and clusters [25], for future studies in hyperthermia [26] for biomedical applications.

2. Experimental

2.1. Sample Preparation

All the reagents used in this work are of analytical purity, purchased from SIGMA-ALDRICH. The magnetic nanoparticles (NPs) were synthesized according to the hydrothermal co-precipitation method according to the one proposed by Tourinho et al. [27,28]. The initial aqueous solutions of (0.5 M) $\text{MnCl}_2\cdot 4\text{H}_2\text{O}$ and (0.5 M) $\text{FeCl}_3\cdot 6\text{H}_2\text{O}$ were mixed in alkaline medium with $\text{CH}_3\cdot\text{NH}_2$ (methylamine) at 100 °C. Then, a treatment with $\text{Fe}(\text{NO}_3)_3$ at 100 °C was carried out to guarantee the stability of the particles and to avoid their degradation in acidic media [29]. This surface treatment induces iron enrichment of the nanoparticles, thus creating a superficial layer of maghemite $\gamma\text{-Fe}_2\text{O}_3$ that surrounds the particle core made of a nickel ferrite. The synthesized ferrofluid has volumetric fraction $\phi = 2.0\%$ and $\text{pH} = 2$.

2.2. Measurements

The chemical composition of NPs is checked by determination of Mn and Fe concentrations with atomic absorption spectroscopy (AAS) technique. Both measurements with a Thermo Scientific Spectrometer model S series AA, with specific lines are chosen for each metal (Mn (279.5 nm) and Fe (248.3 nm/372.0 nm)) to avoid interference effects.

In order to obtain the size distribution and polydispersity and aspects of the morphology of our nanoparticles, measurements were taken using an Electron Transmitting Electron Microscope (MET) JEOL 100CX2. The sample was diluted, then placed on the ultrasound for 1 h and then placed in the sample port until the liquid evaporated.

The magnetic characterization of ferrofluid is performed using the vibrating sample magnetometer (VSM; PPMS, Quantum Design model 6000). The magnetization curves are obtained as a function of the applied field (up to 9000 kA/m) at room temperature.

The colloidal characterization was performed SAXS measurements at the Brazilian Synchrotron Light Laboratory (LNLS), in the beamline D11A-SAXS1 UVX ring. With wavelength of $\lambda = 1.7556 \text{ \AA}$, it is q the scattering vector between $5.08 \times 10^{-3} < q < 0.124 \text{ \AA}^{-1}$ ($q = 4\pi\sin(\theta/2)/\lambda$, θ is angle

scattering). The detector used was MarCCD165 2D and the sample-detector distance was 2.250 m. The sample holder of quartz capillaries had a diameter of 1.5 mm and for the measurements with applied magnetic field two Neodymium magnets [7] were used, perpendicular to the X-ray beam. The data were corrected by the contribution of the empty sample holder and the scattering of water.

3. Theoretical Background

For magnetic characterization of the particles, let us consider an assemble of independent single-domain grains with a magnetic moment $\mu = \pi m_s d^3 / 6$; where m_s is the magnetization of the NPs. In the presence of an external field, the liquid matrix with the suspended particles behaves as an ideal superparamagnet and the ferrofluid magnetization is given by the Langevin law: $M = m_s \phi, L(\zeta) = \coth \zeta - \zeta^{-1}, \zeta = \mu_0 \mu H / k_B T$, with ϕ the ferrite volume fraction, k_B the Boltzmann constant T the temperature. This equation shows that at $H = 0$ the magnetization is zero. As the field H is turned on, the magnetic moments tend to align in the field direction so that at high fields, M saturates at $m_s \phi$. For polydisperse ferrofluids and considering particle size distributions, weighting Langevin with log-normal distribution.

The analysis of SAXS experimental data was first using the unified global equation proposed by Beaucage et al. [17,18]. This equation incorporates the Guinier and Porod boundaries and allows information on parameters such as radius of gyration, log-normal polydispersity index and the exponent associated with the interfacial regime, fractal dimensions of clusters. Thus, in Equation (1), the first level of structure corresponds to the larger scatter object, i.e., the primary clusters composed of some NPs, its size is comprised by means of the radius of gyration, Rg_1 . The second level of structure is relative to the isolated spherical NPs, Rg_2 .

$$I(q) = G_1 e^{-q^2 Rg_1^2 / 3} + B_1 e^{-q^2 Rg_2^2 / 3} h_1^{(-P_1)} + G_2 e^{-q^2 Rg_1^2 / 3} + B_2 h_2^{(-P_2)} \tag{1}$$

where $h_1 = q / [\text{erf}(q[(Rg_1)] / \sqrt{6})]^3, h_2 = q / [\text{erf}(q[(Rg_2)] / \sqrt{6})]^3$, where $\text{erf}(x)$ is an error function, G_1 and G_2 are the pre-factors of Guinier, B_1 and B_2 , the pre-factors of Porod, P_1 and P_2 are the indices of the power law, for the respective regions of analysis. The mean radius R_{part} and the polydispersion in size (σ) of individual spherical particles are determined by the following expressions.

$$R_{part} = \sqrt{\left(\frac{5}{3}\right)} Rg_2 \exp(7\sigma^2), \sigma = \sqrt{\frac{\ln\left(\frac{B_2 Rg_2^4}{1.62 G_2}\right)}{12}} \tag{2}$$

In the case of the correlated particles, we have the insertion of one more multiplicative term $S(q)$ to Equation (1). $S(q)$ is the structure factor, ξ is the mean of the distances between the correlated objects, and k is the degree of correlation [30,31].

$$S(q) = \frac{1}{1 + k \left(3 \frac{\sin(q\xi) - (q\xi)\cos(q\xi)}{(q\xi)^3} \right)} \tag{3}$$

The function of distance distribution in pairs $p(r)$, corresponds to the Fourier transform of the signal of $I(q)$. The function reveals valuable information about the shape of the scatter object and the size, allowing a more intuitive interpretation of the intensity profile [32].

$$p(r) = r^2 / (2\pi^2) \int I(q) \frac{\sin(qr)}{qr} q^2 dq \tag{4}$$

First principles in the theoretical radius of gyration of n -particles that make up the clusters takes into account the association of the moment of inertia of each spherical particle ($I = (2MR^2)/5$) with mean radius of R and mean mass M and associated with the theorem of parallel axes for the formulation

of the spatial configuration of the clusters. The symbol I_{xx} , I_{yy} , I_{zz} are known as the moments of inertia of a 3D rigid body about the respective axes.

$$I_{xx} = \int (y^2 + z^2) dm, \tag{5a}$$

$$I_{yy} = \int (x^2 + z^2) dm, \tag{5b}$$

$$I_{zz} = \int (x^2 + y^2) dm, \tag{5c}$$

$$I_{xx} + I_{yy} + I_{zz} = 2MRg^2. \tag{5d}$$

For a system of more particles, we combine the Equation (5d) for each particle together with the theorem of parallel axes. For the case without magnetic field application. Equation (6b) describes the case $n = N_{clust} = 10$ particles, and $d_{H=0}$ is a mean distance between particle.

$$I \sum_{i=1}^{n=N_{clust}} \left(\frac{2}{5}MR_i^2 + \frac{Md_i^2}{4} + \frac{2}{5}MR_i^2 + \frac{Md_i^2}{4} + \frac{2}{5}MR_i^2 + \frac{Md_i^2}{4} \right) = 2(nM)Rg_{H=0}^2, \tag{6a}$$

$$Rg_{H=0}^2 \approx \frac{3}{5}R_{H=0}^2 + \frac{9d_{H=0}^2}{10}. \tag{6b}$$

For the case with applied magnetic field, we do not have as much rotational freedom, since the objects are aligned with the magnetic field, in this way we have two of the three components with calculation equal to zero. Equation (7b) describes the a case $N_{clust}^{\perp,\parallel}$ of the $n = 10$ particles, and $d_{\parallel,\perp}$ is a mean distance between particles in the projections parallel and perpendicular to the field, the general mean distance between particles can be found as $d_{H\neq 0} = \sqrt{(d_{\parallel}^2 + d_{\perp}^2)}$.

$$I \sum_{i=1}^{n=N_{clust}^{\perp,\parallel}} \left(0 + 0 + \frac{2}{5}MR_{i,\perp,\parallel}^2 + \frac{Md_{i,\perp,\parallel}^2}{4} \right) = 2(nM)Rg_{\perp,\parallel}^2, \tag{7a}$$

$$Rg_{\perp,\parallel}^2 \approx \frac{R_{\perp,\parallel}^2}{5} + \frac{7d_{\perp,\parallel}^2}{3}. \tag{7b}$$

4. Results and Discussions

The results show that in the chemical characterization performed, after the coprecipitation step, the stoichiometry of the core NPs does not correspond to that of an ideal ferrite. Thus, we write the chemical formula as $MnFe_2O_{4+\delta}$ ($Fd\bar{3}m$ space group symmetry) to obtain the stoichiometry of naked NPs, δ is the oxidation parameter. Other complex materials also have the similar behavior, Campi et al. (2019) [9] makes analysis of perovskite $La_2CuO_{4+\delta}$ (with $\delta = 0.1$ has orthorhombic $Fmmm$ space group symmetry) with space resolved $S\mu$ XRD (Scanning X-ray micro-Diffraction). An excess of positive charges occurs due to the oxidation of Mn^{+2} to Mn^{+3} in the synthesis process, in order to balance exactly the extra positive charge that appears in the formula is inserted a δ parameter of 0.48 to adjust the electronegativity. In recent works by Martins et al. [23] and Moreira et al. [33], the mean valence of manganese in ferrites synthesized by coprecipitation was determined. Several analyzes were performed, including the X-ray Absorption Near Edge Structure (XANES) analysis with the Linear Combination Fitting (LFC) method of Mn_3O_4 , Mn_2O_3 and MnO_2 oxides. It was found that there is more Mn^{+3} than other valence states Mn^{+2} and Mn^{+4} , resulting in an average oxidation of +3. Such analysis collaborates with the result of LFC was the absorption edge shift determined with the first derivative of the normalized X-ray absorption spectroscopy (XAS) signal. The Rietveld refinements of X-ray Powder Diffraction (XPD) and Neutron Powder Diffraction (NPD) by Martins and the Pair Distribution Function (PDF) made by Moreira, both performed for non-stoichiometric ferrites,

showed an increase in the oxygen occupancy rate. The value of χ_m further undergoes a reduction of its value with the formation of the iron rich shell (γ -Fe₂O₃). Thus, we find a value of $\chi_m = 0.22$ much smaller than an ideal ferrite that is 0.33. Based on the non-stoichiometric core of the manganese ferrite and the magnetite shell and using the results of the χ_m , it was possible to determine the thickness of the shell ($th = 0.57$ nm). The calculation of the molar fraction is given by, $\chi_m = [\text{Mn}]/([\text{Mn}] + [\text{Fe}])$. Studies correlated to this mechanism of the core-shell model were reported in the works of Gomes et al. [34], Martins et al. [23], and Pilates et al. [26].

Figure 1a presents the TEM picture of the sample and shows that the NPs are roughly spherical. The NPs size distribution was estimated by measuring the size of about 300 particles, using a log normal law of size distribution which corresponds to the probability density that a particle has a diameter $d^{TEM} = 7.1$ nm, with a standard deviation $\sigma^{TEM} = 0.25$. Figure 1b presents the normalized room temperature magnetization curve for NPs; the full line is the best fit of Langevin, adjusting the experimental data, which allowed us to determine $m_s = 172$ kA/m, $d^{mag} = 6.8$ nm and $\sigma^{mag} = 0.26$.

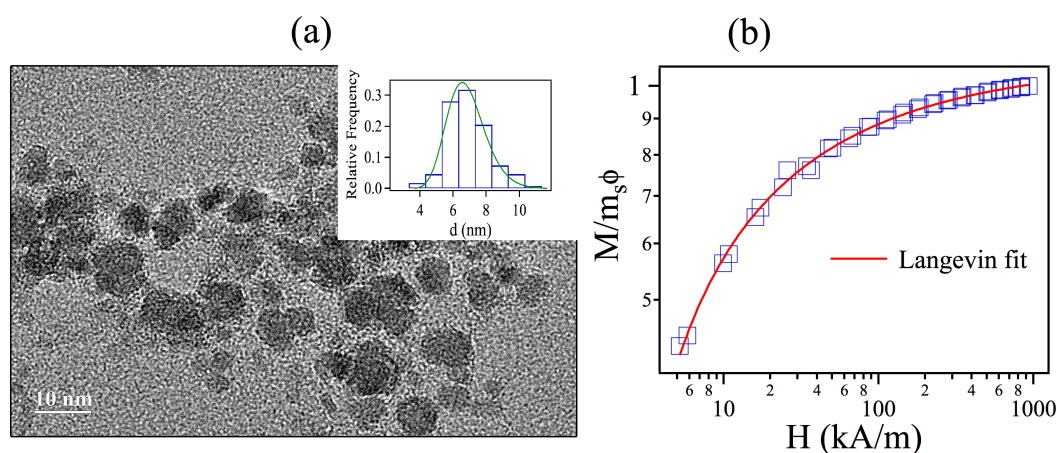


Figure 1. (a) TEM picture of the nanoparticles (NPs), the insert display with size distribution histogram adjusted with (—) log-normal distribution, and (b) Reduced magnetization of (□) sample as function of the applied magnetic field. The solid line (—) is the fit to the data using the Langevin formalism.

Figure 2 shows the two-dimensional patterns ((a) 2D isotropic pattern; (b) 2D anisotropic pattern) at Small-Angle X-ray Scattering of the ferrofluid sample with manganese ferrite core-shell type (MnFe₂O_{4+δ}@γ-Fe₂O₃) nanoparticles [23]. Figure 2b shows the external magnetic field of intensity is $H = 538$ mT applied perpendicular to the direction of propagation of the incident beam. The curve 1D, intensity scattering $I(q)$ is calculated after averaging in a constant radius, ring with the aid of FIT2D software [35]. In relation to the two-dimensional, anisotropic, we don't integrate the entire surface of the image to obtain the curves 1D, $I(q, H = 0)$, and yes, we delimit two distinct integration regions. These regions correspond to azimuthal averages over $\pm 5^\circ$ in the image, in the perpendicular directions $I_{\perp}(q, H)$ and parallel $I_{\parallel}(q, H)$ to the applied magnetic field [36,37]. Angular sector was used in the integration of the 2D pattern in order not to have a radial intensity variation with the angle, since for larger angles we could have regions with intensity variations due to a radial anisotropy of the intensity in the integration area (Figure 2b).

In Figure 3 we show the small angle scattering curves, with the Guinier and Porod components for the two levels of structure as presented in Equation (1). In the Guinier region, all curves have a non-zero inclination, there is a behavior of globally attractive systems, probably associated to the presence of primary clusters of NPs. In case of a system without interaction, we would have a plateau in the region of Guinier, that is, $I(q) \sim q^{-0}$. In Figure 3c the curve of $I_{\perp}(q, H)$, the slope is less pronounced than $I_{\parallel}(q, H)$ (Figure 3b) and $I(q, H = 0)$ (Figure 3a), that is, it is a less attractive system. In $I_{\perp}(q, H)$ there is a correlation peak at $q^{peak} \sim 0.034 \text{ \AA}^{-1}$, characteristic of a globally repulsive system with a mean

distance between the primary clusters of $\xi^{peak} \sim 181 \text{ \AA}$ ($\xi^{peak} = 2\pi/q^{peak}$). In the curves with a large q we observe the law of power q^{-4} corresponding to the interface hard of nanoparticles

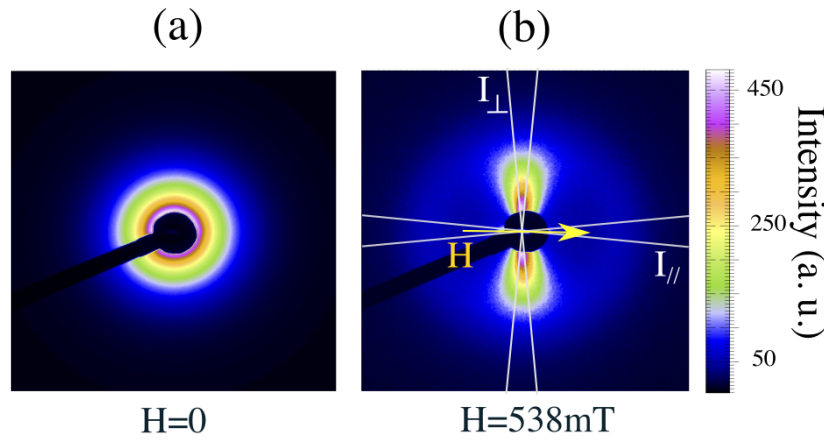


Figure 2. Two-dimensional X-ray scattering patterns for ferrofluid based on manganese ferrite nanoparticles. (a) isotropic pattern, with no applied magnetic field; (b) anisotropic pattern, Ferrofluid with external magnetic field application of $H = 538 \text{ mT}$, the white lines limit are azimuthal averages over $\pm 5^\circ$ in directions perpendicular and parallel to the magnetic field to obtain 1D curves shown in Figure 3b,c.

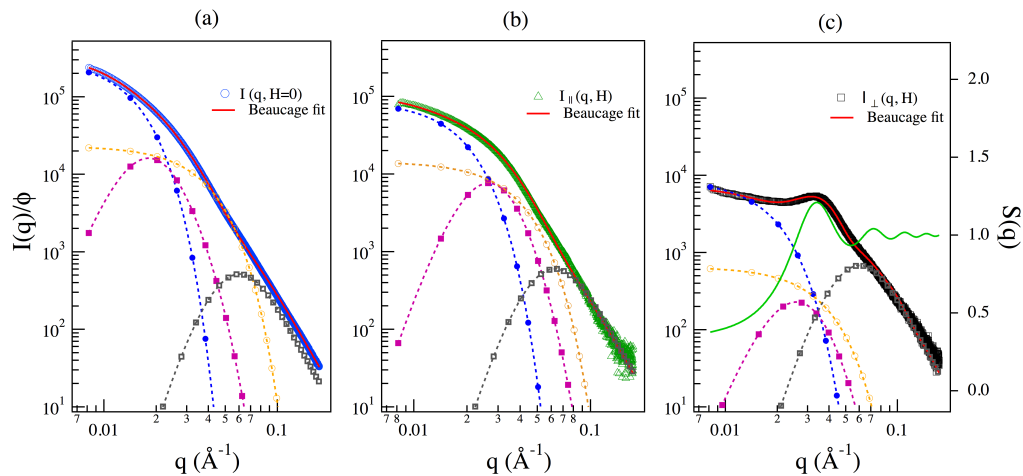


Figure 3. The X-ray scattering curves normalized by the volumetric fraction. Better fit results, following the (—) unified Beaucage expression described in the text. Contribution of the (—●—) Guinier and (—■—) components related to the first level of the structure corresponding to the largest object in the dispersion, (—○—) Guinier and (—□—) Porod components referring to the second structure level are relative to the isolated NPs, and (—) $S(q)$ is the structure factor. (a) $I(q, H = 0)$ scattering curve without external field application; (b) $I_{\parallel}(q, H)$ scattering curve obtained in the integration of the 2D pattern in the direction parallel to the magnetic field; (c) $I_{\perp}(q, H)$ scattering curve perpendicular to the magnetic field.

The number of NPs per cluster involved in the first structure level is $N_{clust} = (Rg_1/Rg_2)^{P_1}$, using the values Rg_1 and Rg_2 Table 1, which respectively describes the clusters and individual particles by the Beaucage model (Equation (1)). The values found were $N_{clust} \sim 10$, $N_{clust}^{\parallel} \sim 5.3$ and $N_{clust}^{\perp} \sim 1.8$, respectively, without field, field applied parallel and orthogonally. Only with the correlation of the values found of N_{clust}^{\parallel} and N_{clust}^{\perp} is it possible to obtain information about the cluster in the field action.

Table 1. Fitting parameters obtained the SAXS data analysed using the Beaucage model. The parameters Rg_1 and P_1 refer to the clusters; Rg_2 and P_2 , the individual particles; k and ξ parameters of the structure factor and N_{clust} are related to the number of nanoparticles per clusters.

	Rg_1 [Å]	P_1	Rg_2 [Å]	P_2	k	ξ [Å]	N_{clust}
$I(q, H = 0)$	105	2.7	46	3.95	-	-	~ 10
$I_{\parallel}(q, H)$	81.5	2.79	45	4.00	-	-	~ 5.3
$I_{\perp}(q, H)$	57.5	2.3	45	3.85	2.01	181	~ 1.8

In Figure 4, we have the schematic representation of the spatial configuration of the NPs, so we have that, the same quantitative of particles have reorganized, repositioning in the direction of the field, the fact that collaborates for such effect and the relation found $N_{clust}^{\parallel} \times N_{clust}^{\perp} \approx N_{clust}$. In Figure 4a,b the radial distribution analysis of the scattering curves obtained by means of Equation (4) allowed a maximum size for the scattering object; in the case, without field, we have $D_{max}^{H=0;p(r)} = 210 \text{ \AA}$.

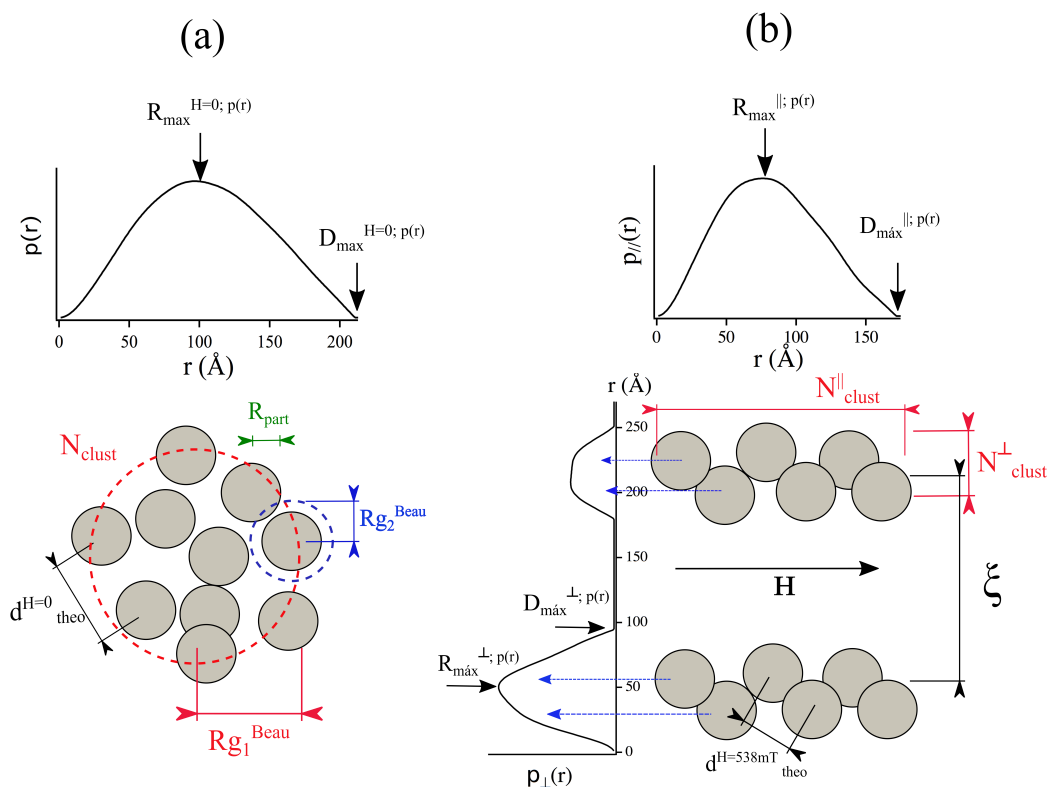


Figure 4. Parameter distribution function (—) corresponding to the Fourier transform to the Small Angle X-ray Scattering (SAXS) curves and the schematic drawing of the spatial configuration of the NPs, taking into account the information obtained by the Beaucage model and the curves of $p(r)$ and the theoretical radius of gyration ($d_{theo}^{H=538mT}$, Equation (7b); $d_{theo}^{H=0mT}$, Equation (6b)) and the theoretical distance calculated with and without field; $D_{max}^{H=0,\parallel,\perp;p(r)}$ determination the size of the scattered object, that $R_{max}^{H=0,\parallel,\perp;p(r)}$ is the average of the scatter object; $N_{clust}^{\parallel,\perp}$ and N_{clust} is the number of NPs in the cluster with and without field; $Rg_{1,2}^{Beau}$ is the radius of the gyration): (a) $H = 0 \text{ T}$; (b) with field, the formation of chains of particles with a mean inter-cluster distance of $\xi \sim 181 \text{ \AA}$.

In the case with the applied magnetic field, we have a rearrangement of the spatial configuration of the object due to the action of the field, the particles are oriented in the direction of the field and, in the perpendicular direction, the objects have a distancing behavior for the formation of chains in the

direction of the field. We then see that $D_{max}^{\parallel;p(r)} = 160 \text{ \AA}$ and, in the direction perpendicular to the field, two regions were determined; the first $D_{max}^{\perp;p(r)} = 90 \text{ \AA}$ and then another $D_{max}^{\perp;p(r)} = 70 \text{ \AA}$, with a range of $\xi^{p(r)} \sim 180 \text{ \AA}$.

For a better understanding, see the schematic illustration in Figure 4. The result $D_{max}^{H=0;p(r)} > D_{max}^{\parallel;p(r)}$, is given by the alignment of the dipole moments of the NPs, thus increasing the magnetic interaction, consequently decreasing the distance between particles.

In Figure 4a and Table 2, in a system without field, $p^{H=0}(r)$ is quasi-symmetric indicating an object scattered approximately in a sphere, this is due to the profile of the curve being almost symmetric, with radius of the clusters of $R_{clust}^{H=0;p(r)} \sim 90 \text{ \AA}$. In Figure 4b, the distribution $p^{\perp}(r)$ in the direction of the field, of $R_{clust}^{\parallel;p(r)} \sim 74 \text{ \AA}$, at $p^{\parallel}(r)$, in the direction of the field perpendicular to the field, the radius of the clusters is $R_{clust}^{\perp;p(r)} \sim 51 \text{ \AA}$. The analysis of the radial distribution perpendicular and parallel allows us to obtain the dimensions of the thickness and the length of the clusters, as represented schematically in Figure 4.

Table 2. $D_{max}^{H=0,\parallel,\perp;p(r)}$ is the maximum of the pair distribution, with $R_{clust}^{H=0,\parallel,\perp;p(r)}$ being the maximum point of $p(r)^{H=0,\parallel,\perp}$, respectively. The $Rg_{theo}^{H=0,\parallel,\perp}$ is the theoretical radius of gyration of the clusters that is calculated by the moments of inertia and $d_{theo}^{H=0,\parallel,\perp}$ and the distance between particles in the clusters.

	$D_{max}^{H=0,\parallel,\perp;p(r)}$ [Å]	$R_{clust}^{H=0,\parallel,\perp;p(r)}$ [Å]	$Rg_{theo}^{H=0,\parallel,\perp}$ [Å]	$d_{theo}^{H=0,\parallel,\perp}$ [Å]
$H = 0$	210	90	103.2	105
	160	74	84.0	53
⊥	90	51	58.2	37

We see a decrease in D_{max} for the signs $p^{\parallel}(r)$ and $p^{\perp}(r)$, this is due to the reorganization of the scattering objects before the field action. We also have that due to the limitation of the degrees of freedom for the scattering objects on the action of the magnetic field, it is possible to verify by the values of the radius of gyration by the Beaucage method (Table 2) is $Rg_1^{H=0;Beau} = 105 > Rg_1^{\parallel;Beau} = 81.5 > Rg_1^{\perp;Beau} = 57.5 \text{ \AA}$. To better understand this relationship, the calculation of the theoretical radius of gyration was performed using Equations (6b) and (7b). In the case of the system without field: $Rg_{theo}^{H=0} = 103.2 \text{ \AA}$ and $d_{theo}^{H=0} = 105 \text{ \AA}$; and with field, we have due to the limitation, degrees of rotational freedom. Thus, two of these components of Equation (7a) are zero, $Rg_{theo}^{\parallel} = 84 \text{ \AA}$ and $d_{theo}^{\parallel} = 53 \text{ \AA}$ and $Rg_{theo}^{\perp} = 58.2 \text{ \AA}$ and $d_{theo}^{\perp} = 37 \text{ \AA}$. The values determined for the radius of gyration by the method of Beaucage are in agreement with those determined by the theoretical calculation. The average distance between the particles with magnetic field is obtained by means of the projections of the distances obtained by the analysis of the signal in the parallel and perpendicular direction:

$$d_{theo}^{H=538mT} = \sqrt{(d_{theo}^{\parallel 2} + d_{theo}^{\perp 2})} = \sqrt{(53^2 + 37^2)} = 64.63 \text{ \AA}.$$

It is observed that $d_{theo}^{H=0} > d_{theo}^{H=538 mT}$, this is due to the spatial reorganization of the scattering objects, since there is a greater alignment of the dipoles moments of the NPs towards the field, resulting in greater intraparticle interaction. The average radius of the individual particles $R_{part} = 35 \text{ \AA}$ and the polydispersity $\sigma = 0.24$ were determined using the expressions for spherical scattering objects (slope in $I(q) \sim q^{-4}$) in the Beaucage Equation (2). The values for diameter and polydispersion in the techniques of morphological characterization (TEM) and magnetic (magnetization curve) are in good agreement with that determined using the SAXS technique. We see that the diameter $d_{part} = (2R_{part})$, d^{mag} , $d^{TEM} \approx 70 \text{ \AA}$, and polydispersion σ_{part} , σ^{mag} , $\sigma^{TEM} \approx 0.25$.

5. Conclusions

It was very promising to study the local structure of these dispersions using the SAXS technique, since it was possible to have access to the spatial organization of the nanoparticles in clusters in two regimes with and without applied magnetic field. In this sense, one can better measure the size of the clusters and the individual nanoparticles. In addition to information about the mean distance between particles and between the chains of particles when the field is applied. The calculation performed for theoretical radius of gyration for the clusters, even if simplistic, proved to be very consistent with the values found in the analyzes using the unified global equation and the radial distribution function. The results showed the behavior of a globally repulsive colloidal system in the direction perpendicular to the field and globally attractive in the direction of the magnetic field. For the repulsive system, we have that the distance between clusters is $\xi^{peak}, \xi^{P(r)}, \xi^{Beau} \approx 180 \text{ \AA}$. The analysis of the globally attractive curves helped us to understand the dimensions of the clusters, as to the form and quantity of particles involved in their formation. In this way, we find that the number of particles in the clusters follows the relation, $N_{clust}^{||} \times N_{clust}^{\perp} \approx N_{clust}$ reaffirming the spatial reconfiguration of the particles on the action of the magnetic field. It was also evidenced the good agreement of the values for diameter and polydispersion in the techniques of morphological characterization (TEM) and magnetic with the technique of SAXS. We intend to study, in the light of this work, the relation of the volumetric fraction and the intensity of the magnetic field applied in the formation of the clusters.

Funding: This work was supported by Brazilian agencies, the National Council for Scientific and Technological Development through the National Institute of Science and Technology of Complex Fluids (INCT-FCx-CNPq—grant numbers 465259/2014-6 and 400849/2016-0), the Coordination for the Improvement of Higher Education Personnel (CAPES) and the Federal District Research Foundation (FAPDF—grant numbers 0193-001376/2016, 0193-001194/2016 and 0193.001569/2017).

Acknowledgments: This research used resources of the Brazilian Synchrotron Light Laboratory (LNLS), an open national facility operated by the Brazilian Centre for Research in Energy and Materials (CNPEM) for the Brazilian Ministry for Science, Technology, Innovations and Communications (MCTIC). The D11-SAXS1 beamline staff is acknowledged for the assistance during the experiments. Special thanks to R. Aquino and J. Depeyrot for technical assistance. Thanks to Aldenora M. O. Paula for textual review. Thanks to the post doctorate program CAPES/COFECUB, grant contract BEX 7288/14-0.

Conflicts of Interest: The author declares no conflict of interest.

Abbreviations

The following abbreviations are used in this manuscript:

SAXS Small-Angle X-ray Scattering
LNLS Brazilian Synchrotron Light Laboratory

References

1. Papell, S.S. Low Viscosity Magnetic Fluid Obtained by the Colloidal Suspension of Magnetic Particles. U.S. Patent 3215572, 2 November 1965.
2. Rosensweig, R.E.; Kaiser, R. *Study of Ferromagnetic Liquid, Phase I*; NTIS Rep. No. NASW-1219; NASA Office of Advanced Research and Technology: Washington, DC, USA, 1967.
3. Rosensweig, R.E. *Ferrohydrodynamics*; Cambridge University Press: Cambridge, UK; London, UK, 1985.
4. Beeran, A.E.; Fernandez, F.B.; Nazeer, S.S.; Jayasree, R.S.; John, A.; Anil, S.; Vellappally, S.; Al Kheraif, A.A.A.; Varma, P.R.H. Multifunctional nano manganese ferrite ferrofluid for efficient theranostic application. *Colloids Surf. B Biointerfaces* **2015**, *136*, 1089–1097. [[CrossRef](#)] [[PubMed](#)]
5. Pankhurst, Q.A.; Thanh, N.T.K.; Jones, S.K.; Dobson, J. Progress in applications of magnetic nanoparticles in biomedicine. *J. Phys. D Appl. Phys.* **2009**, *22*, 224001. [[CrossRef](#)]
6. Fu, Z.; Xiao, Y.; Feoktystov, A.; Pipich, V.; Appavou, M.; Su, Y.; Feng, E.; Jina, W.; Bruckel, T. Field-induced self-assembly of iron oxide nanoparticles investigated using small-angle neutron scattering. *Nanoscale* **2016**, *8*, 18541–18550. [[CrossRef](#)] [[PubMed](#)]

7. Rozynek, Z.; Jozefczak, A.; Knudsen, K.D.; Skumiel, A.; Hornowski, T.; Fossum, J.O.; Timko, M.; Kopcansky, P.; Koneracka, M. Structuring from nanoparticles in oil-based ferrofluids. *Eur. Phys. J. E* **2011**, *34*. [[CrossRef](#)] [[PubMed](#)]
8. Campi, G.; Poccia, N.; Joseph, B.; Bianconi, A.; Mishra, S.; Lee, J.; Roy, S.; Agung Nugroho, A.; Buchholz, M.; Braden, M.; et al. Direct Visualization of Spatial inhomogeneity of Spin Stripes Order in $\text{La}_{1.72}\text{Sr}_{0.28}\text{NiO}_4$. *arXiv* **2019**, arXiv:1905.02124.
9. Campi, G.; Bianconi, A. Evolution of Complexity in Out-of-Equilibrium Systems by Time-Resolved or Space-Resolved Synchrotron Radiation Techniques. *Condens. Matter* **2019**, *4*, 32. [[CrossRef](#)]
10. Wandersman, E.; Chushkin, Y.; Dubois, E.; Dupuis, V.; Robert A.; Perzynski, R. Field induced anisotropic cooperativity in amagnetic colloidal glass. *Soft Matter* **2015**, *11*, 7165. [[CrossRef](#)] [[PubMed](#)]
11. Myrovali, E.; Maniotis, N.; Makridis, A.; Terzopoulou, A.; Ntomprougkidis, V.; Simeonidis, K.; Sakellari, D.; Kalogirou, O.; Samaras, T.; Salikhov, R.; et al. Arrangement at the nanoscale Effect on magnetic particle hyperthermia. *Sci. Rep.* **2016**, *6*, 37934. [[CrossRef](#)]
12. Abenojar, E.C.; Wickramasinghe, S.; Bas-Concepcion, J.; Samia, A.C.S. Structural effects on the magnetic hyperthermia properties of iron oxide nanoparticles. *Prog. Nat. Sci. Mater. Int.* **2016**, *26*, 440–448. [[CrossRef](#)]
13. Serantes, D.; Simeonidis, K.; Angelakeris, M.; Chubykalo-Fesenko, O.; Marciello, M.; Del Puerto Morales, M.; Baldomir, D.; Martinez-Boubeta, C. Multiplying Magnetic Hyperthermia. Response by Nanoparticle Assembling. *J. Phys. Chem. C* **2014**, *118*, 5927–5934. [[CrossRef](#)]
14. Martinez-Boubeta, C.; Simeonidis, K.; Makridis, A.; Angelakeris, M.; Iglesias, O.; Guardia, P.; Cabot, A.; Yedra, L.; Estradé, S.; Peiró, F.; et al. Learning from nature to improve the heat generation of iron-oxide nanoparticles for magnetic hyperthermia applications. *Sci. Rep.* **2013**, *3*, 1652. [[CrossRef](#)] [[PubMed](#)]
15. Mehdaoui, B.; Tan, R.P.; Meffre, A.; Carrey, J.; Lachaize, S.; Chaudret, B.; Respaud, M. Increase of magnetic hyperthermia efficiency due to dipolar interactions in low-anisotropy magnetic nanoparticles: Theoretical and experimental results. *Phys. Rev. B* **2013**, *87*, 174419. [[CrossRef](#)]
16. Bañobre-López, M.; Teijeiro, A.; Rivas, J. Magnetic nanoparticle-based hyperthermia for cancer treatment. *Rep. Pract. Oncol. Radiother.* **2013**, *18*, 397–400. [[CrossRef](#)] [[PubMed](#)]
17. Beaucage, G.; Schaefer, D.W. Structural studies of complex systems using small-angle scattering: A unified Guinier/power-law approach. *J. Non-Cryst. Solids* **1994**, *172–174*, 797–805. [[CrossRef](#)]
18. Beaucage, G. Approximations Leading to a Unified Exponential/Power-Law Approach to Small-Angle Scattering. *J. Appl. Cryst.* **1995**, *28*, 717. [[CrossRef](#)]
19. Beaucage, G. Small-Angle Scattering from Polymeric Mass Fractals of Arbitrary Mass-Fractal Dimension. *J. Appl. Cryst.* **1996**, *29*, 134. [[CrossRef](#)]
20. Beaucage, G. Determination of branch fraction and minimum dimension of mass-fractal aggregates. *Phys. Rev. E* **2004**, *70*, 031401. [[CrossRef](#)]
21. Beaucage, G.; Kammler, H.K.; Pratsinis, S.E. Particle size distributions from small-angle scattering using global scattering functions. *J. Appl. Cryst.* **2004**, *37*, 523. [[CrossRef](#)]
22. Paula, F.L.O.; Depeyrot, J.; Fossum, J.O.; Tourinho, F.A.; Aquino, R.; Knudsen, K.D.; da Silva, G.J. Small-angle X-ray and small-angle neutron scattering investigations of colloidal dispersions of magnetic nanoparticles and clay nanoplatelets. *J. Appl. Cryst.* **2007**, *40*, 269–273. [[CrossRef](#)]
23. Martins, F.H.; da Silva, F.G.; Paula, F.L.O.; Gomes, J.A.; Aquino, R.; Mestnik-Filho, J.; Bonville, P.; Porcher, F.; Perzynski, R.; Depeyrot, J. Local Structure of Core-Shell $\text{MnFe}_2\text{O}_{4+\delta}$ Based Nanocrystals: Cation Distribution and Valence States of Manganese Ions. *J. Phys. Chem. C* **2017**, *121*, 8982–8991. [[CrossRef](#)]
24. Paula, F.L.O.; da Silva, G.J.; Aquino, R.; Depeyrot, J.; Fossum, J.O.; Knudsen, K.; Tourinho, F.A. Gravitational and Magnetic Separation in Self-Assembled Clay-Ferrofluid Nanocomposites. *Braz. J. Phys.* **2009**, *39*, 163–170. [[CrossRef](#)]
25. Castro, L.L.; da Silva, M.; Bakuzis, A.; Miotto, R. Aggregate formation on polydisperse ferrofluids: A Monte Carlo analysis. *J. Magn. Magn. Mater.* **2005**, *293*, 553–558. [[CrossRef](#)]
26. Vanessa, P.; Cabreira, R.G.; Gomide, G.S.; Coppola, P.; Silva, F.G.; Paula, F.L.O.; Perzynski, R.; Goya, F.G.; Aquino, R.; Depeyrot, J. Core/Shell Nanoparticles of Non-Stoichiometric Zn-Mn and Zn-Co Ferrites as Thermosensitive Heat Sources for Magnetic Fluid Hyperthermia. *J. Phys. Chem. C* **2018**, *122*, 3028. [[CrossRef](#)]
27. Tourinho, F.A.; Franck, R.; Massart, R.; Perzynski, R. Synthesis and magnetic properties of manganese and cobalt ferrite ferrofluids. *Prog. Colloid Polym. Sci.* **1989**, *79*, 128–134.

28. Tourinho, F.A.; Franck, R.; Massart, R. Aqueous ferrofluids based on manganese and cobalt ferrites. *J. Mater. Sci.* **1990**, *25*, 3249–3254. [[CrossRef](#)]
29. Gomes, J.A.; Sousa, M.H.; Tourinho, F.A.; Aquino, R.; Depeyrot, J.; Dubois, E.; Perzynski, R. Synthesis of Core-Shell Ferrite Nanoparticles for Ferrofluids: Chemical and Magnetic Analysis. *J. Phys. Chem. C* **2008**, *112*, 6220–6227. [[CrossRef](#)]
30. Zaioncz, S.; Dahmouche, K.; Soares, B.G. SAXS Characterization of New Nanocomposites Based on Epoxy Resin/Siloxane/MMA/Acrylic Acid Hybrid Materials. *Macromol. Mater. Eng.* **2010**, *295*, 243–255. [[CrossRef](#)]
31. Beaucage, G.; Ulibarri, T.; Black, E.P.; Schaefer, D.W. *Hybrid Organic-Inorganic Composites*; Mark, J.E., Lee, C.Y.-C.; Bianconi, P.A., Eds.; ACS Symposium Series 585; American Chemical Society: Washington, DC, USA, 1985; p. 97.
32. Svergun, D.I.; Koch, M.H.; Timmins, P.A.; May, R.P. *Small Angle X-Ray and Neutron Scattering from Solutions of Biological Macromolecules*; Oxford University Press: Oxford, UK, 2013.
33. Moreira, A.F.L.; Paula, F.L.O.; Depeyrot, J. Evidence of Structural Distortions in Mixed Mn-Zn ferrite. *IOSR J. App. Phys.* **2019**, *11*, 36–44. [[CrossRef](#)]
34. Gomes, J.A.; Azevedo, G.M.; Depeyrot, J.; Mestnik-Filho, J.; Paula, F.L.O.; Tourinho, F.A.; Perzynski, R. Structural, Chemical, and Magnetic Investigations of Core-Shell Zinc Ferrite Nanoparticles. *J. Phys. Chem. C* **2012**, *116*, 24281–24291. [[CrossRef](#)]
35. Available online: <http://www.esrf.eu/computing/scientific/FIT2D> (accessed on 21 July 2014).
36. Mériquet, G.; Cousin, F.; Dubois, E.; Boué, F.; Cebers, A.; Farago, B.; Perzynski, R. What Tunes the Structural Anisotropy of Magnetic Fluids under a Magnetic Field? *J. Phys. Chem. B* **2006**, *110*, 4378–4386. [[CrossRef](#)]
37. Robbes, A.S.; Cousin, F.; Meneau, F.; Dalmas, F.; Boué, F.; Jestin, J. Nanocomposite Materials with Controlled Anisotropic Reinforcement Triggered by Magnetic Self-Assembly. *Macromolecules* **2011**, *44*, 8858–8865. [[CrossRef](#)]



© 2019 by the author. Licensee MDPI, Basel, Switzerland. This article is an open access article distributed under the terms and conditions of the Creative Commons Attribution (CC BY) license (<http://creativecommons.org/licenses/by/4.0/>).